Knowledge-graph-based cell-cell communication inference for spatially resolved transcriptomic data with SpaTalk

Xin Shao[1, 3, †], Chengyu Li[3, †], Haihong Yang[2, 4, †], Xiaoyan Lu[3], Jie Liao[3], Jingyang Qian[3], Kai Wang[1], Junyun Cheng[3], Penghui Yang[3], Huajun Chen[2, 4, *], Xiao Xu[1, 5, *], Xiaohui Fan[1, 3, 5, *]

[1]Key Laboratory of Integrated Oncology and Intelligent Medicine of Zhejiang Province, Department of Hepatobiliary and Pancreatic Surgery, Affiliated Hangzhou First People's Hospital, Zhejiang University School of Medicine, Hangzhou 310006, China.

[2]Hangzhou Innovation Center, Zhejiang University, Hangzhou 310058, China

[3]Pharmaceutical Informatics Institute, College of Pharmaceutical Sciences, Zhejiang University, Hangzhou 310058, China

[4]College of Computer Science and Technology, Zhejiang University, Hangzhou 310027, China

[5]Westlake Laboratory of Life Sciences and Biomedicine, Hangzhou 310003, China.

[†]These authors should be regarded as Joint First Authors

*Corresponding author: Dr. Huajun Chen (huajunsir@zju.edu.cn), Dr. Xiao Xu (E-mail: zjxu@zju.edu.cn) and Dr. Xiaohui Fan (E-mail: fanxh@zju.edu.cn, Tel/Fax: 86-571-88208596)

Abstract

Spatially resolved transcriptomics (ST) provides genetic information in space toward elucidation of the spatial architecture in intact organs and the spatially resolved cell-cell communications mediating tissue homeostasis, development, and disease. To facilitate inference of spatially resolved cell-cell communications from ST data, we here present SpaTalk, which relies on a graph network and knowledge graph to model and score the ligand-receptor-target signaling network between spatially proximal cells, decomposed from ST data through a non-negative linear model and spatial mapping between single-cell RNA-sequencing and ST data. The performance of SpaTalk benchmarked on public single-cell ST datasets was superior to that of existing cell-cell communication inference methods. SpaTalk was then applied to STARmap, Slide-seq, and 10X Visium data, revealing the in-depth communicative mechanisms underlying normal and disease tissues with spatial structure. SpaTalk can uncover spatially resolved cell-cell communications for single-cell and spot-based ST data universally, providing new insights into spatial inter-cellular dynamics.

Introduction

Cell-cell communications via secreting and receiving ligands frequently occur in multicellular organisms, which is a vital feature involving numerous biological processes[1]. Standard algorithms for inferring cell–cell communications mediated by ligand–receptor interactions (LRIs) primarily incorporate a database of known LRIs and single-cell transcriptomic data by delineating cell populations and their lineage relationships[2, 3]. One common strategy is to integrate the abundance of ligands and receptors for the inference of signals from senders to receivers based on the premise that highly co-expressed ligands and receptors are likely to mediate inter-cellular communications[4, 5]. Another strategy applies the downstream targets triggered by LRIs in receivers to enrich and score the ligand-receptor-target (LRT) signaling network[6-8]. Although single-cell transcriptomic data can provide information on the genes contributing to cell-cell communications, the spatial information of cells is inevitably lost when dissociating tissues into single cells, thereby hindering the extension of current tools to investigate cell-cell communications in tissues with spatial structure[9].

Recent technological advances in spatially resolved transcriptomics (ST) benefiting from spatial barcoding and imaging-based approaches have enabled the measurement of whole or mostly whole transcriptomes while retaining the spatial information[10, 11], which have been increasingly adopted to generate new insights in the biological and biomedical domains, with dramatically improved accuracy and reliability in the inference of spatially proximal cell-cell communications[12]. Given the space-constrained nature of juxtacrine and paracrine signaling, such spatial gene expression information is vital to understand cell-cell communications mediating tissue homeostasis, development, and disease[13, 14].

Several methods have recently emerged to decode the mechanisms of cell-cell communications in space[15]. For example, Giotto utilizes preferential cell neighbors over single-cell ST datasets for each pair of cell types with an enrichment test to evaluate the likelihood of a given LRI based on proximal co-expressing cells and infer cell-cell communication in space[16]. SpaOTsc applies structured optimal transport mapping between scRNA-seq and ST data to assign a spatial position for each cell, resulting in a cell–cell distance as a transport cost to infer the ligand–receptor signaling network that mediates space-constrained cell–cell communication[17]. However, Giotto and SpaOTsc are limited to infer inter-cellular communications over single-cell ST data rather than the spot-based ST data and between paired cell types rather than paired cells. It still lacks of methods that can infer and visualize spatially resolved cell-cell communications at single-cell resolution over ST data to date, posing a great challenge for decoding spatial inter-cellular dynamics underlying disease pathology.

To address this challenge, we herein proposed SpaTalk, a spatially resolved cell-cell communication inference method by creatively integrating the principles of the ligand–receptor proximity and ligand–receptor–target (LRT) co-expression to model and score the LRT signaling network between spatially proximal cells relying on the graph network and knowledge graph approaches[18]. The performance of SpaTalk was evaluated on benchmarked datasets with remarkable superiority over other methods. By applying to STARmap[19], Slide-seq[20, 21], and 10X Visium[22] datasets, SpaTalk revealed the in-depth communicative mechanisms underlying normal and disease tissues with spatial structure. Collectively, these results demonstrate SpaTalk as a useful and universal method that can help to uncover spatially resolved cell–cell communications for both single-cell and spot-based ST data, providing insights into the understanding

of spatial inter-cellular dynamics in tissues.

Results

Overview of the SpaTalk method. Fig. 1 provides an overview of the workflow for developing and testing SpaTalk, comprising two main components: (1) dissect the cell-type composition of ST data and (2) infer spatially resolved cell–cell communications over decomposed single-cell ST data (Fig. 1a). In the first component, the non-negative linear model (NNLM)[23-25] was applied to decode the cell-type composition for a single-cell or spot-based ST data matrix using the scRNA-seq data matrix with k cell types as the underlying reference. By incorporating Lee's multiplicative iteration algorithm and relative entropy loss[25], the model was trained with default hyperparameters until convergence, producing a weight matrix representing the optimal proportion of cell types for each cell/spot. For single-cell ST data, the cell type with the maximum weight was assigned to label each cell. For spot-based ST data, the cell types with different weights were used as the reference to project the cells from scRNA-seq data onto the spatial spot (Fig. 1b). Through random sampling and deep iteration processes, the optimal cellular combination that most resembled the spatial spot was refined to reconstruct the single-cell ST data for spot-based ST data.

The second component of SpaTalk is to infer spatially resolved cell–cell communications and downstream signal pathways. To identify possible communications among cells mediated by LRIs, the principles of ligand–receptor proximity and ligand–receptor–target (LRT) co-expression were incorporated based on a recent review[12]. In detail, the KNN algorithm is first applied to each cell in space to construct the cell graph network. For the ligand of the sender (cell type A) and the

receptor of the receiver (cell type B), the number of LRI pairs is obtained from the graph network by counting the 1-hop neighbor nodes of receivers for each sender. A permutation test filters and scores the significantly enriched LRIs, generating the inter-cellular score (Fig. 1c).
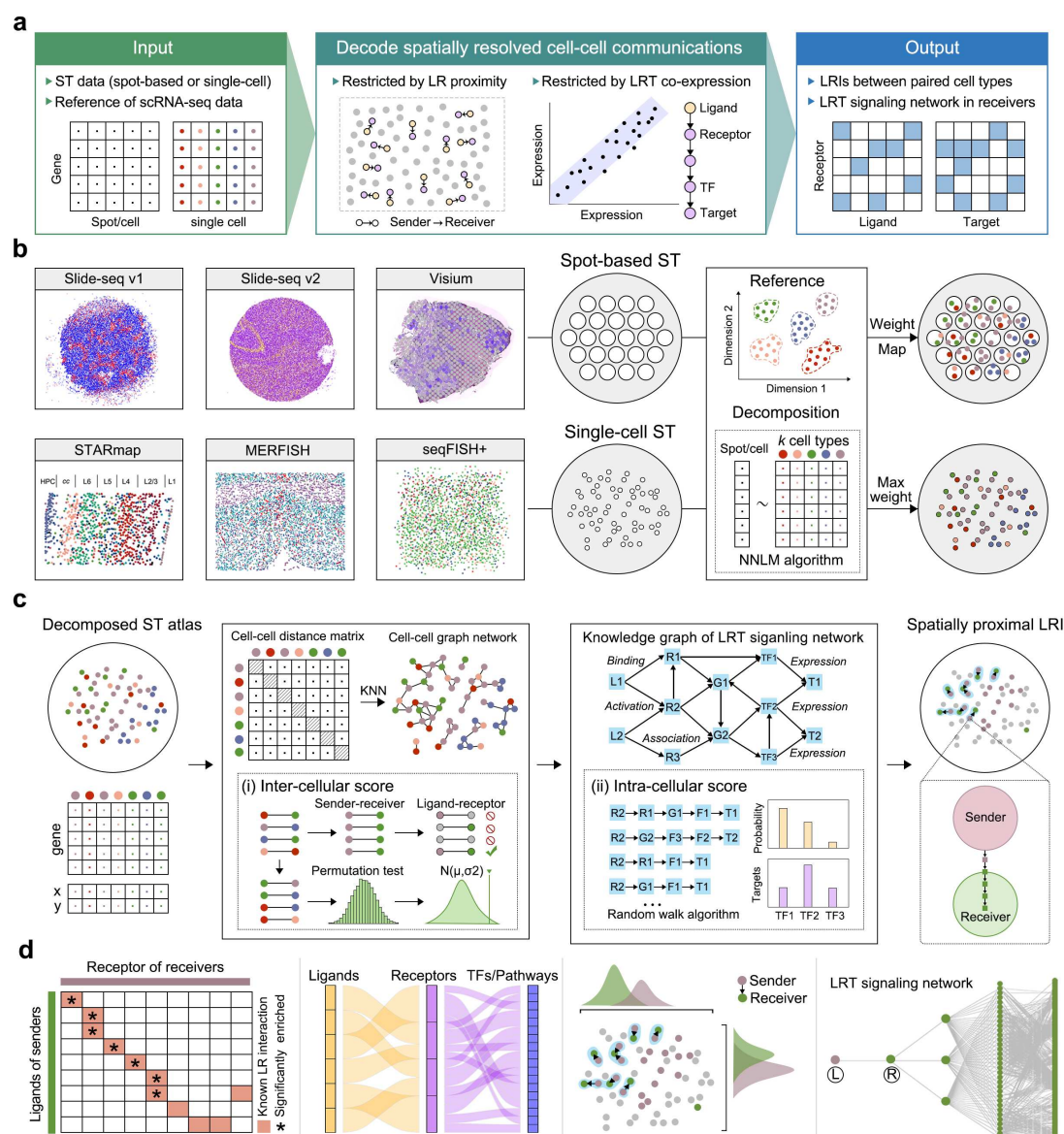

Fig. 1 Workflow of the SpaTalk method and visualization. a Overview of SpaTalk, including the input, intermediate process of decoding spatially resolved cell–cell communications, and output. **b** Conceptual framework of cell-type decomposition with SpaTalk. Five different spatial technologies and datasets were selected and analyzed: spot-based ST data (Slide-seq and 10X Visium) and single-cell ST data (STARmap, MERFISH, and seqFISH+). NNLM was used to dissect the optimal proportion of cell types for the projection of cells from scRNA-seq reference data onto the spatial cells/spots, generating single-cell ST data with known cell types. **c** Schematic representation of SpaTalk to infer spatially resolved cell–cell communications

mediated by LRIs. The inter-cellular and intra-cellular scores were obtained and combined from the cell–cell graph network and the LRT-knowledge graph (KG), respectively, by integrating the KNN, permutation test, and random walk algorithms. L, ligand; R, receptor; TF, transcription factor; T, target. **d** Visualization of spatially resolved cell–cell communications, including a heatmap, Sankey plot, and diagram of the LRI from senders to receivers in space, as well as ligand-receptor-target (LRT) signaling pathways over the reconstructed single-cell ST data.

The knowledge graph (KG) was then introduced to model the intracellular signal propagation process. In practice, LRIs from CellTalkDB[26], pathways from Kyoto Encyclopedia of Genes and Genomes (KEGG) and Reactome, and TFs from AnimalTFDB[27] were integrated to construct the LRT-KG, wherein the weight between entities represents the co-expressed coefficient. Taking the receptor as the query node, we incorporated the random walk algorithm[28] into the LRT-KG to filter and score the downstream activated TFs and calculate the intracellular score of the LRI from senders to receivers. Inter-cellular and intra-cellular scores are combined to rank the LRIs that mediate spatially resolved cell-cell communications.

SpaTalk also includes numerous visualization functions to characterize the cell-type composition and spatially resolved cell–cell communications, such as the diagram of the LRI from senders to receivers in space and LRT signaling pathways, over the reconstructed single-cell ST data (Fig. 1d). Five broad ranges of different spatial technologies and corresponding representative datasets were analyzed and visualized: spot-based ST data (Slide-seq[20, 21] and 10X Visium[22]) and single-cell ST data (STARmap[19], MERFISH[29], and seqFISH+[30]).

Performance comparison of SpaTalk with other methods. The cell-type decomposition by SpaTalk is the foundation for subsequent analyses. To evaluate its performance, four single-cell ST datasets from the mouse cortex, hypothalamus,

olfactory bulb, and sub-ventricular zone were utilized (Supplementary Fig. 1a). All cells were split according to the fixed spatial distance and then merged into simulated spots as the benchmark datasets (Fig. 2a). The quality of predicted cell-type decompositions and expression profiles was evaluated by Pearson's correlation coefficient and the root mean square error (RMSE) based on the ground truth, wherein SpaTalk exhibited fantastic performance over the benchmark datasets (Supplementary Fig. 1b, c). Although the majority of existing cell-type deconvolution methods (RCTD[31], Seurat[32], SPOTlight[33], deconvSeq[34], and Stereoscope[35]) can achieve a decent correlation coefficient and low RMSE on spot deconvolution, SpaTalk outperformed these methods on most benchmark datasets with the top-ranked performance, except for the MERFISH dataset (Fig. 2b). The MERFISH dataset only includes 155 genes, whereas the STARmap and seqFISH+ datasets cover 1020 and 10,000 genes per cell, respectively, suggesting that SpaTalk is potentially more effective for spatial data with higher gene coverage.

We next compared the performance of SpaTalk with that of existing cell–cell communication inference methods (Supplementary Fig. 2a). Consequently, most methods exhibited a large fraction of overlapped predictions with the rest of the methods despite the different number of inferred cell-cell communications (Supplementary Fig. 2b, c), indicating the reproducible inference across these methods. Regarding the inferred LRIs (Supplementary Fig. 2d), we reasoned that the spatial distances of the inferred LRI between sender–receiver pairs will be shorter than those between all cell–cell pairs and thus the inferred LRI will be more co-expressed in local space as cells that are close are more likely to signal (Fig. 2c). The one-sided Wilcoxon test was performed to evaluate the spatial proximity significance of the inferred LRIs,

and the co-expressed percentage of the LRI was calculated as the co-expression level using the cell–cell graph network. Although most LRIs inferred by other methods showed significantly closer spatial distances between sender–receiver pairs than that between all cell–cell pairs, superior performance of SpaTalk was observed, ranking first for both evaluation indices for STARmap datasets (Fig. 2d). Similarly, SpaTalk obtained a higher median $-\log_{10}P$ value and co-expression percent on the seqFISH+ OB and SVZ datasets but not for SpaOTsc (Fig. 2e).
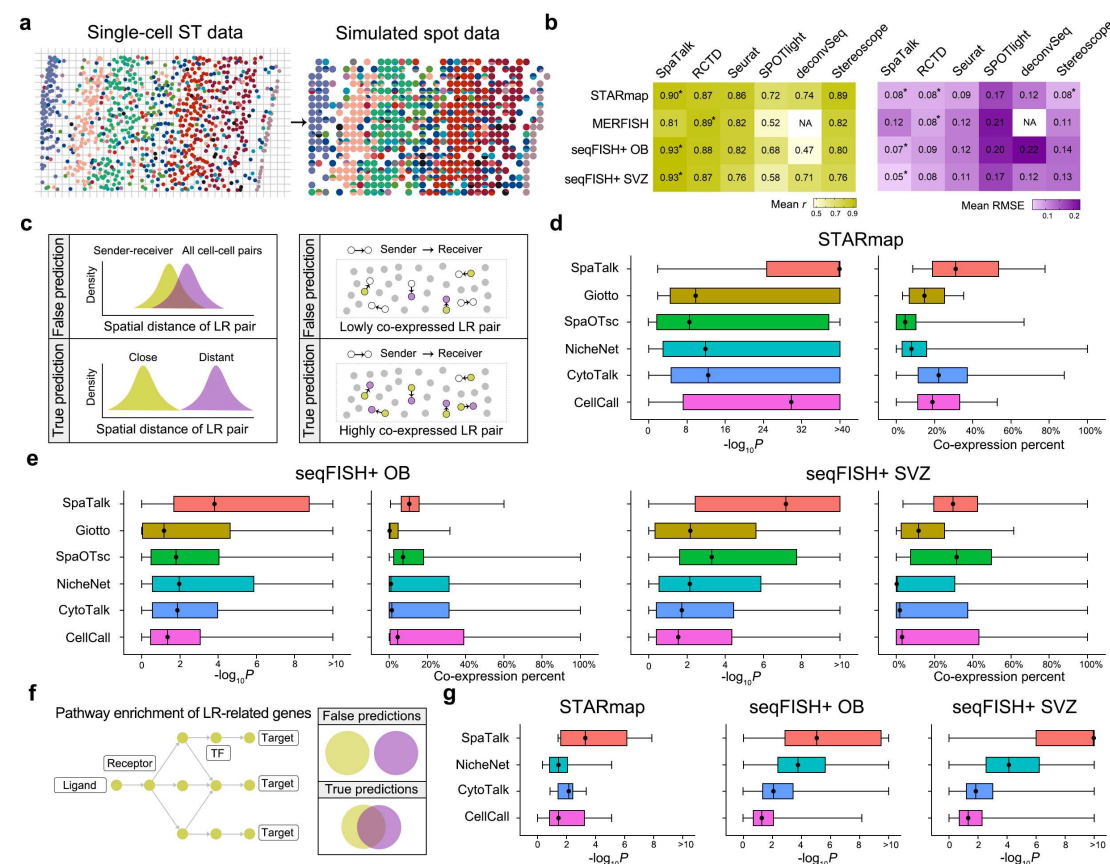

Fig. 2 Superior performance of SpaTalk over existing methods. a Schematic diagram for generating simulated spot data. Cells were split according to the fixed spatial distance and then merged for the single-cell ST data with known cell types. **b** Performance comparison of SpaTalk with other existing cell-type deconvolution methods (RCTD, Seurat, SPOTlight, deconvSeq, Stereoscope). The asterisk represents the top-ranked method for each dataset. NA, not available. **c** Schematic illustration of the procedure and rationale for single-cell ST data to evaluate predicted LRIs that mediate spatially resolved cell–cell communications. **d** and **e** Performance comparison of SpaTalk with existing cell–cell communication inference methods (Giotto, SpaOTsc, NicheNet, CytoTalk, and CellCall) on the STARmap and seqFISH+ datasets. The *P* value

represents the difference of spatial distances between sender–receiver and all cell–cell pairs assessed with the Wilcoxon test. **f** Schematic illustration of the procedure and rationale for single-cell ST data to evaluate predicted downstream target and pathways underlying LRIs. **g** Performance comparison of SpaTalk on the inferred downstream targets with other methods (NicheNet, CytoTalk, and CellCall) over the STARmap and seqFISH+ datasets. The *P* value represents the significance of enriched pathways or biological processes from the KEGG and Reactome databases using inferred downstream targets with the Fisher exact test.

We compared the performance of SpaTalk for inference of intra-cellular signal pathways of the receiver cell type triggered by the LRI with those of NicheNet[6], CytoTalk[7], and CellCall[8] that also infer the downstream targets of LRIs. We reasoned that a more accurate method would be more likely to enrich the receptor-related biological processes or pathways using the inferred downstream target genes in the receiver cell type (Fig. 2f); hence, the Fisher-exact test was adopted for pathway enrichment analysis with the KEGG and Reactome databases on target genes in receivers. The target genes inferred by all methods enriched the most intra-cellular pathways or biological processes triggered by the inter-cellular LRI (Fig. 2g). Nevertheless, SpaTalk exhibited the top-ranked performance over three benchmarked datasets, exceeding other existing methods in inference of the LRT signal network.

Identification of signal transmission among neurons and non-neuronal cells. SpaTalk was first applied to investigate and visualize the cell–cell communications over the STARmap ST dataset of the mouse visual cortex (Fig. 3a), including data of 1020 sequenced genes for 973 cells in space covering the spatial axis of excitatory neurons (eL2/3, eL4, eL5, eL6, annotated by anatomic cortical layers); *Pvalb*, *Reln*, *Sst*, and *Vip*-expressing neurons; and non-neuronal cells, including astrocytes (Astro), endothelial cells (Endo), microglia (Micro), oligodendrocytes (Oligo), and smooth muscle cells

(SMCs) from layers L1 though L6 to the corpus callosum and hippocampus. As shown in Fig. 3b, SpaTalk identified the spatial signal transmission among excitatory and inhibitory neurons and non-neuronal cells such as *Sst–Sstr2, Inhba–Acvr1c,* and *Cort–Sstr2*. For example, the direct cell–cell communication mediated by the *Sst–Sstr2* interaction was observed between *Sst*-expressing neurons and *Pvalb*-expressing neurons (Supplementary Fig. 3a), which are known to regulate neuron activity via non-synaptic, inter-neuronal communication[36, 37]. Concordantly, these identified LRIs among neurons and non-neuronal cells are associated with multiple biological processes and pathways that play vital roles in the regulation of physiological neural development and the balance of excitatory/inhibitory transmission in the central nervous system[38, 39], including growth hormone synthesis, secretion, and action; neuroactive ligand-receptor interaction; signaling by activin; and the transforming growth factor (TGF)-beta signaling pathway (Fig. 3c).

Notably, Astro were relatively abundant across space of the L5 layer and colocalized with numerous excitatory neurons, exhibiting direct cell–cell communication with eL2/3, eL5, and eL6 (Supplementary Fig. 3b). Given the *Cort–Sstr2* interaction between eL5 and Astro, eL5 highly expressed and secreted the CORT ligand to interact with the SSTR2 receptor on Astro with a highly overlapped distribution density of eL5 and Astro in the constrained space, wherein the spatial distances of *Cort* and *Sstr2* in eL5–Astro pairs were significantly closer than those in all cell–cell pairs (Fig. 3d). Focusing on the intra-cellular signal pathway of the *Cort–Sstr2* interaction reconstructed by SpaTalk, two downstream TFs were identified, *Egr1* and *Smad3*, which are involved in canonical TGF-beta signaling, in line with previous findings[40]. Despite the relatively low-rise co-expression of target genes in receivers, the intra-

cellular signal triggered by the *Cort–Sstr2* interaction successfully propagated to the target genes, reaching a high percentage of cells expressing most target genes (Fig. 3e). The Fisher exact test showed significant enrichment with receptor-related pathways (Fig. 3f), indicating the reliability of eL5–Astro communications mediated by the *Cort–Sstr2* interaction.

We then applied SpaTalk to another spot-based ST dataset of the mouse cortex (Slide-seq v2), including 17,545 unique genes among 42,550 spots in space, reaching up to 4000 expressed genes per spot. Leveraging previously published adult mouse cortical cell taxonomy by scRNA-seq data[41] (Supplementary Fig. 3c), SpaTalk reconstructed the spatial transcriptomics atlas at the single-cell resolution for Slide-seq data, which showed consistent spatial localization of neurons and non-neuronal cells across different layers, including the major excitatory and inhibitory neurons and Oligo (Fig. 3g). Compared to STARmap data, oligodendrocyte progenitor cells, and *Igtp*-, *Ndnf*-, and *Smad3*-expressing neurons were also observed in the Slide-seq data. Concordantly, most cell–cell communications in STARmap data were also found in Slide-seq data except for those of distinct cell types in the two datasets (Supplementary Fig. 3d). For example, the eL5–Astro communications mediated by the *Cort–Sstr2* interaction in space and the downstream targets such as SMAD3 were also observed in Slide-seq data (Fig. 3h), suggesting the universality of the spatially resolved cell-cell communications inferred by SpaTalk. In addition, the direct communications among Pvalb neurons, eL6, and Oligo were also significantly enriched, in accordance with the fact that neuron-oligo communication controls the oligodendrocyte function and myelin biogenesis (Supplementary Fig. 3e).
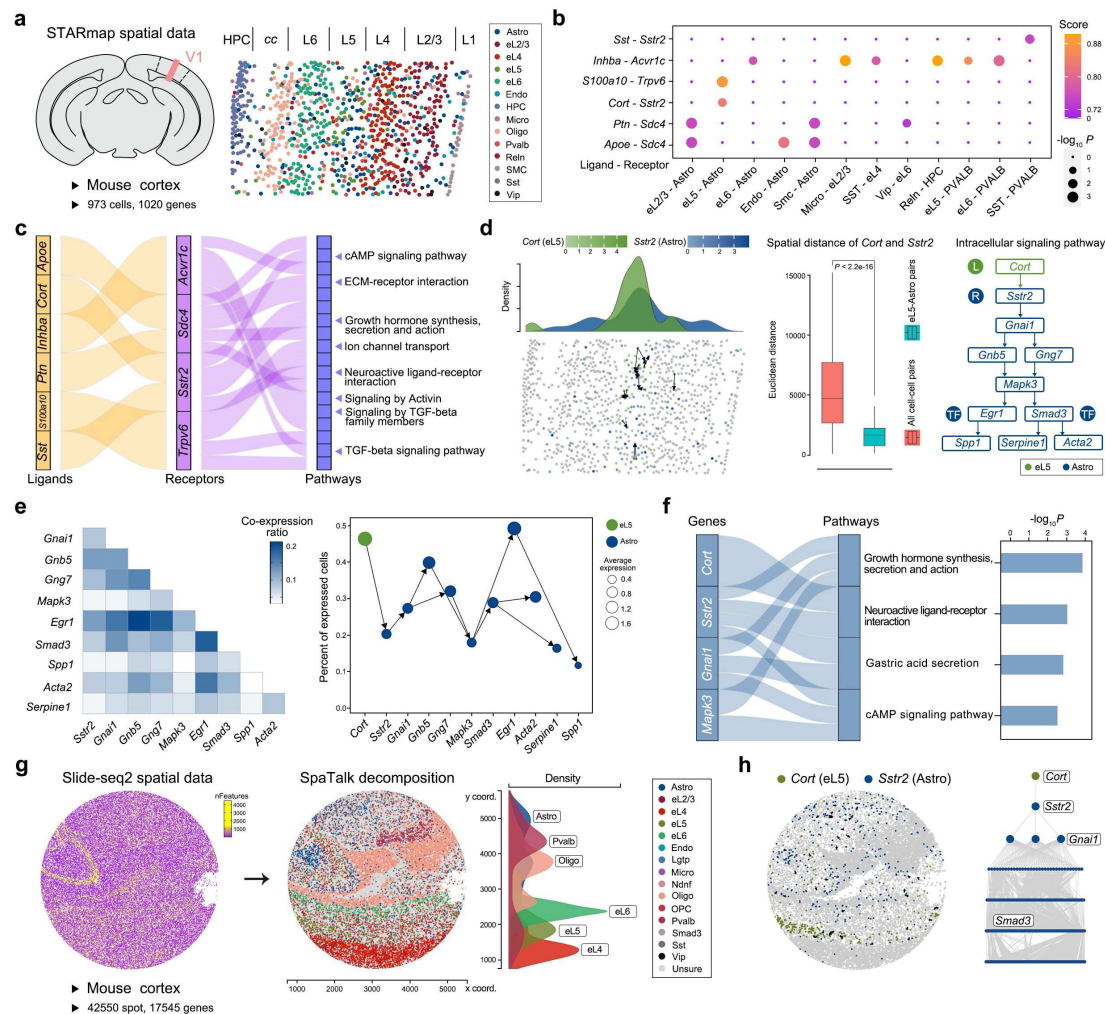
Fig. 3 Identification of spatial inhibitory signal transmission among neurons and non-neuronal cells. a STARmap single-cell ST dataset of the mouse visual cortex involving 973 cells and 1020 genes. Astro, astrocytes; eL2/3, eL4, eL5, eL6, excitatory neuron subtypes; Endo, endothelial cells; HPC, hippocampus; Micro, microglia; Oligo, oligodendrocytes; SMC, smooth muscle cells; cc, corpus callosum. **b** Significantly enriched LRIs that mediate cell–cell communications among neurons and non-neuronal cells inferred by SpaTalk with $P < 0.05$. The P value represents the significance of spatial proximity of LRIs using the permutation test. **c** Sanky plot of the associations among ligands, receptors, and biological processes or pathways in the KEGG and Reactome databases that mediate cell–cell communications in the central nervous system. **d** Spatial distribution and intra-cellular signaling pathways of the *Cort–Sstr2* pairs between the eL5 senders and Astro receivers. P values were calculated with the Wilcoxon test. **e** Co-expression of target genes in receivers and the percentage of expressed cells for target genes. **f** Significantly enriched biological processes and pathways with the ligand-receptor-target genes using the Fisher exact test. **g** Slide-seq spot-based ST dataset of the mouse visual cortex involving 42,550 spots and 22,542 genes. OPC, oligodendrocyte progenitor cell. **h** Communications of eL5–Astro mediated by the *Cort–Sstr2* interaction in space and the intra-cellular signal pathway

inferred by SpaTalk over Slide-seq data.

Metabolic modulation of periportal hepatocytes on pericentral hepatocytes. We applied SpaTalk to the Slide-seq ST dataset of the mouse liver covering 17,545 unique genes among 25,595 spots in space (Fig. 4a). To explore the cell-type composition of Slide-seq data, a mouse liver scRNA-seq reference integrating the non-parenchymal cells from the Mouse Cell Atlas (MCA)[42] and the parenchymal hepatic cells from the GSE125688 dataset[43] were utilized (Supplementary Fig. 4a), containing 6029 cells, including major immune cells such as macrophages (Macro), and the pericentral and periportal hepatocytes. The reconstructed single-cell ST atlas was perfectly accordant with the original outcome obtained by Slide-seq (Fig. 4b), wherein the expression of known marker genes[44] and the percent for each cell type were highly correlated across spots (Supplementary Fig. 4b, c, d), such as the pericentrally and periportally zonated genes *Cyp2e1* and *Pck1* (Fig. 4c). Immune cells were hardly observed in each spot, with pericentral and periportal hepatocytes accounting for the major proportion across spots (Supplementary Fig. 4e); the same phenomenon was observed in recently published ST data of the healthy liver[45].

The cell–cell communications between pericentral and periportal hepatocytes were further explored by SpaTalk (Fig. 4d). Both hepatocyte types secrete and receive multiple ligands for their communication, forming spatially distributed metabolic cascades to cooperatively optimize the metabolic environment. For instance, with the gradient expression of enzymes in sequential lobule layers, pericentral hepatocytes perform the primary steroid, alcohol, and lipid metabolic processes, while periportal hepatocyte mainly carry out the small-molecule and monosaccharide biosynthetic processes, amino acid and triglyceride metabolic processes, and gluconeogenesis (Fig.

4e, f), in line with the variable functions of zonated hepatocytes residing in the central and portal veins[46]. Notably, the periportal hepatocytes substantially expressed more ligands, including epidermal growth factor (*Egf*), transforming growth factor alpha (*Tgfa*), heparin-binding EGF-like growth factor (*Hbegf*), insulin-like growth factor 1 (*Igf1*), and vascular endothelial growth factor A (*Vegfa*), to promote the growth of pericentral hepatocytes. As the blood flows from the portal vein toward the central vein, this could reflect the fact that periportal hepatocytes respire most of the oxygen, leading to decreased oxygen concentrations along the lobule axis; thus, periportal hepatocytes secrete numerous growth factors via paracrine signaling to modulate the pericentral hepatocytes for the prevention of hypoxia and the maintenance and amelioration of pericentrally metabolic functions[46].

Taking the LRI of *Apob–Cd36* as an example, the spatially resolved cell–cell communications between periportal and pericentral hepatocytes mainly occurred across the mid-lobule layers (Fig. 4g). The gene product of *Apob* is an apolipoprotein of chylomicrons and low-density lipoproteins highly involved with the regulation of lipids and fatty acids metabolism through CD36, indicating the modulation of periportal hepatocytes on the metabolic microenvironment sensed by pericentral hepatocytes. From the reconstructed intra-cellular signal propagation network triggered by the *Apob–Cd36* interaction (Fig. 4h), sequential target TFs were activated, including *Ahr* that regulates xenobiotic-metabolizing enzymes such as cytochrome P450, and *Nr1h4* that regulates the expression of genes involved in bile acid synthesis and transport, in agreement with the corresponding module score of pericentral hepatocytes in space (Fig. 4i). The LRT network was also remarkably enriched in the AMPK and PPAR signaling pathways, which play crucial roles in the regulation of energy

and metabolic homeostasis, suggesting the spatially fine-tuned cell–cell communications along the portal–central lobule axis for minimizing risks to pericentral hepatocytes.
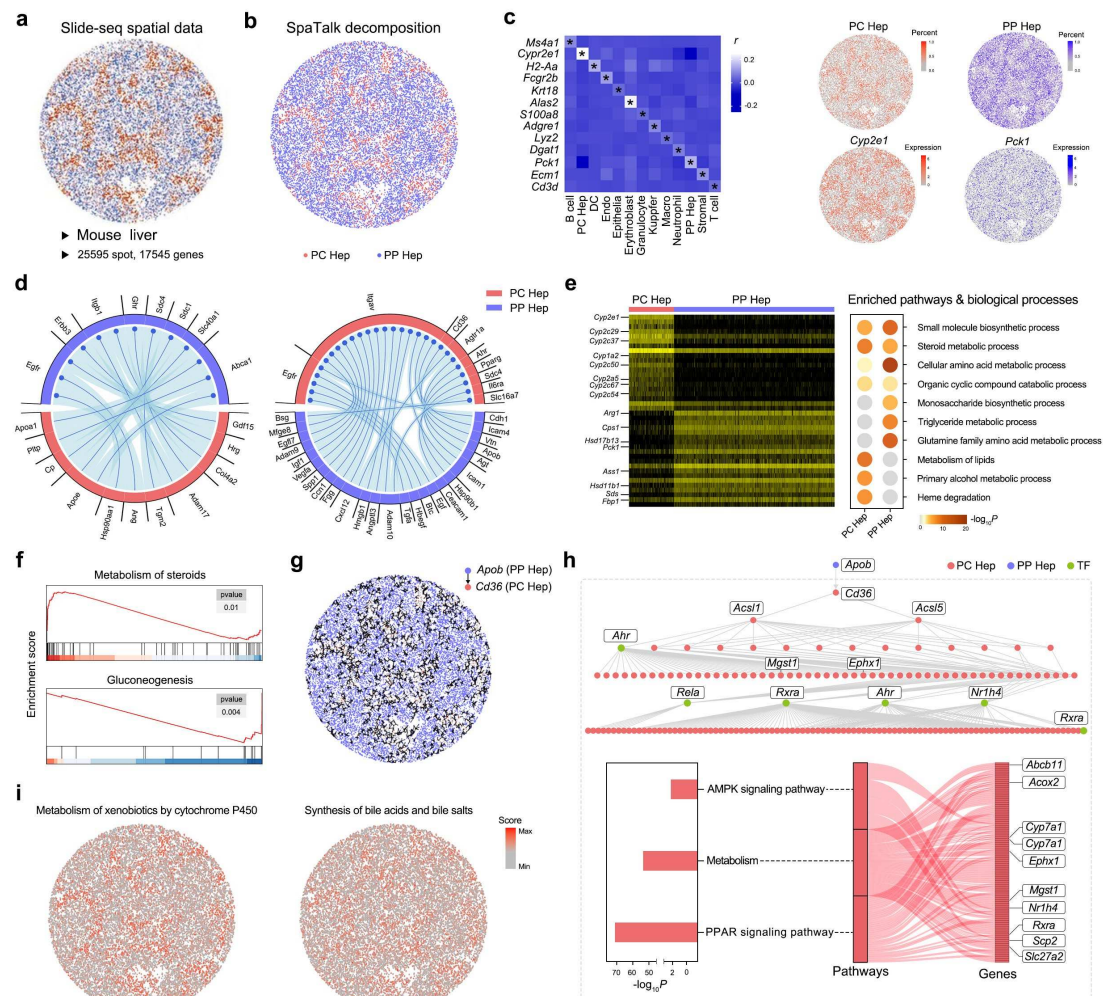

Fig. 4 Modulation of periportal hepatocytes on the metabolic microenvironment sensed by pericentral hepatocytes. a Slide-seq spot-based ST dataset of the mouse liver involving 25,595 spots and 17,545 genes. **b** Cell-type decomposition by SpaTalk. PC, pericentral; PP, periportal; Hep, hepatocytes. **c** Scaled Pearson's correlation coefficients between the expression of known marker genes and the percent for each cell type. DC, dendritic cell; Macro, macrophages. **d** Enriched LRIs that mediate cell–cell communications between pericentral and periportal hepatocytes. **e** Significant differentially expressed genes (DEGs) between periportal and pericentral hepatocytes assessed with the Wilcoxon test and the corresponding significantly enriched biological processes and pathways determined with the Metascape web tool. Representative DEGs are labeled beside the heatmap. **f** Significantly activated pathways in pericentral (up) and periportal (down) hepatocytes determined by Gene Set Enrichment Analysis (GSEA). **g** Communications from periportal hepatocytes to

pericentral hepatocytes mediated by the *Apob–Cd36* interaction in space. **h** Intra-cellular signal pathway inferred by SpaTalk over Slide-seq data and the significantly enriched pathways over the ligand-receptor-target network. **i** Inferred module score of each hepatocyte type over the pathway signatures determined with Seurat.

Spatial characterization of cell types over 10X Visium data. Given the widely used 10X Visium tool in ST studies, we applied SpaTalk to a human skin squamous cell carcinoma (SCC) ST dataset published by Ji et al.[22], who profiled SCC and matched normal tissues via 10X scRNA-seq and used Visium to identify a tumor-specific keratinocyte (TSK) in the tumor (Fig. 5a). Using the matched SCC scRNA-seq data of patient 2 as reference, the optimal cell-type composition for each spot was deconvoluted by SpaTalk, which exhibited a similar characterization with that histologically assessed from hematoxylin and eosin-stained frozen sections (Fig. 5b). The percent of TSK inferred by our method was compared to the TSK score based on markers (e.g., MMP10, PTHLH, LAMC2, and IL24) defined by Ji et al. across 646 spots (Fig. 5c). A high correlation between the TSK percent and score was observed (Fig. 5d). Moreover, the percent of inferred cell types was prominently associated with the expression of known marker genes, indicating the accuracy of SpaTalk for cell-type decomposition (Supplementary Fig. 5a, b).

Next, we reconstructed the single-cell ST profile by assuming a total of 30 cells in each spot according to a recent review[12], which covered the main epithelial cells, including differentiating, cycling, and basal keratinocytes; melanocytes; fibroblasts (FB); Endo; natural killer (NK) cells; and T cells (Fig. 5e). Despite the asymmetrical distribution for most cell types, TSK, FB, and Endo showed specific patterns of locations in space, which were highly adjacent in some tumor areas (Fig. 5f), forming direct cell–cell communications in the tumor microenvironment (TME). By filtering cells from the TSK leading spots (score ≥ 0.8), we found that TSKs reside within a fibrovascular niche,

resulting in high colocalization of TSKs, FB, and Endo at the TSK leading spots (Fig. 5g), in line with the previous findings[22]. Moreover, we used SpaTalk to investigate the cell-type composition over the ST data of another SCC patient. Despite a low percentage across 621 spatial spots, most TSKs centered on a handful of corner spots in space, exhibiting a highly consistent distribution with TSK scores (Fig. 5h and Supplementary Fig. 5c). Unsurprisingly, the fibrovascular niche was also observed in the TSK leading spots of patient 10 with clear spatial co-localization (Supplementary Fig. 5d), indicating the close cell–cell communication among TSKs, FB, and Endo in the TME underlying the occurrence and development of SCC.
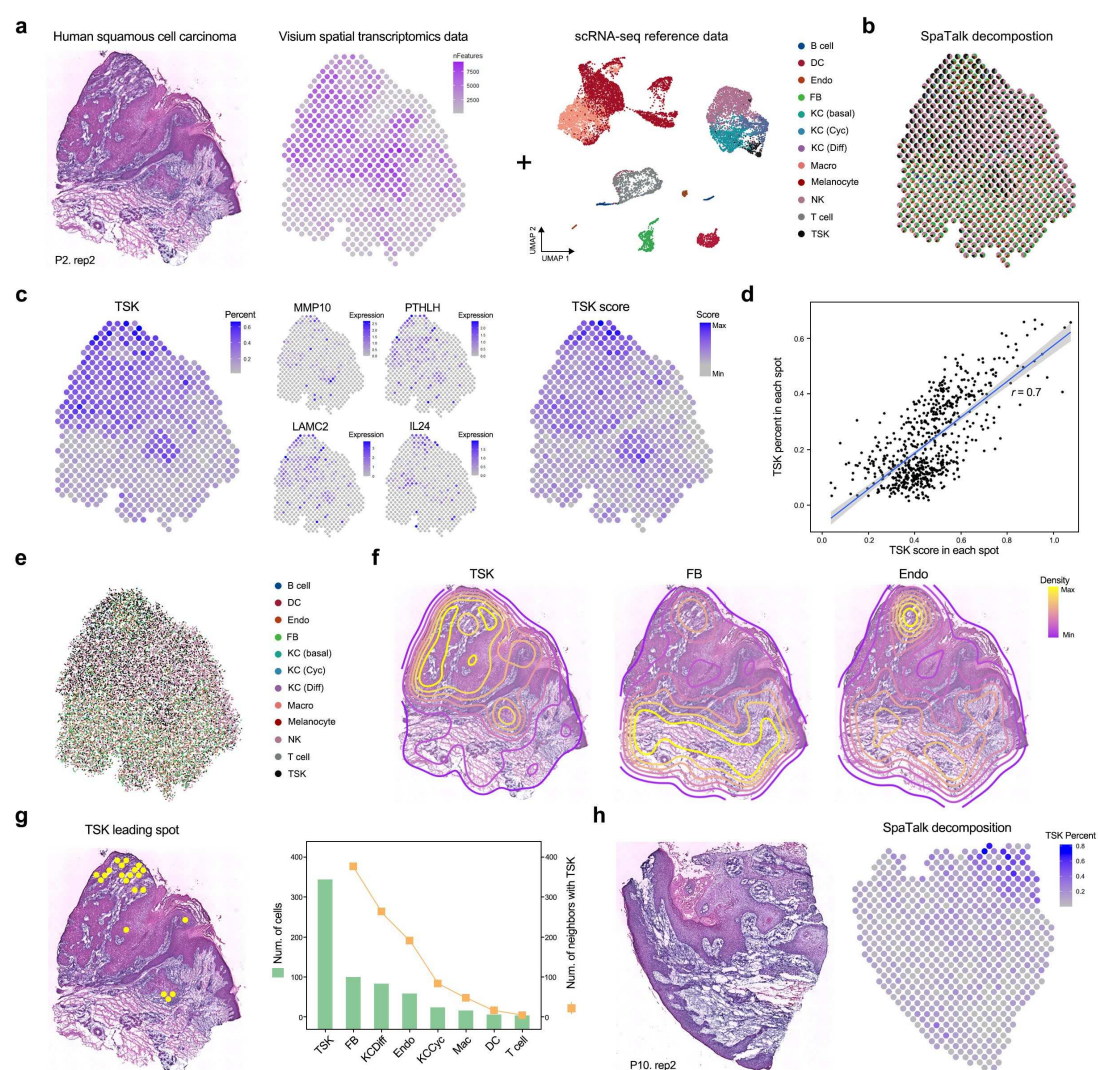

Fig. 5 Spatial characterization of tumor and stromal cells in human squamous cell

carcinoma Visium data with SpaTalk. a Visium spot-based ST dataset of human skin SCC in patient 2 with the matched scRNA-seq dataset involving the main keratinocytes (KC), stromal cells, and immune cells. **b** Cell-type decomposition by SpaTalk. Cyc, cycling; Diff, differentiating; NK, natural killer; FB, fibroblast. **c** TSK percent and TSK score across spatial spots. The expression of known TSK markers is plotted. **d** Pearson's correlation coefficient between the TSK percent and TSK score. **f** Contour plot of TSK, FB, and Endo based on the reconstructed single-cell ST atlas by SpaTalk. **g** TSK leading spots with a TSK score > 0.8 in space. The bar chart represents the number of different cell types and the line chart represents the number of neighbors adjacent to TSKs among the TSK leading spots. **h** Visium spot-based ST dataset of human skin SCC in patient 10 and the cell-type decomposition by SpaTalk showing the percent of TSKs across 621 spatial spots.

Reconstruction of TSK–stroma communications in space. To dissect the underlying LRI mediating the spatially resolved cell–cell communications between TSKs and stromal cells of the fibrovascular niche in the TME, we applied SpaTalk to infer the communications between TSK–FB and TSK–Endo pairs over the decomposed single-cell ST data of SCC in patient 2, including the top-ranked 20 LRIs based on the integrated inter-cellular and intra-cellular scores (Fig. 6a). Consistent with a TSK–fibrovascular niche, prominent TSK signaling to FB and Endo was mediated by several common ligand–receptor pairs, including VEGFA–NPR1, VEGFB–NPR1, PGF–SDC1, and CDH1–ITGAE, associated with tumor angiogenesis. Additionally, TSKs modulate FB through secreting matrix metallopeptidase (MMP)1 and MMP9, which are linked to tumor metastasis via cellular movement and extracellular matrix (ECM) disassembly. Conversely, FB and Endo prominently co-expressed numerous ligands such as MDK, HGF, HMGB1, and THBS1, matching TSK receptors that promote the proliferation and differentiation of TSKs (Fig. 6b). Further supporting TSKs as an epithelial mesenchymal transition (EMT)-like population, SpaTalk predicted that the widely expressed TGFB1 regulates TSKs. TSK receptors corresponding to additional ligands from FB and Endo

included several integrins (e.g., ITGA5 and ITGB6) and nectins (e.g., NECTIN1 and NECTIN2), highlighting other pathways associated with EMT and epithelial tumor invasion[47, 48].
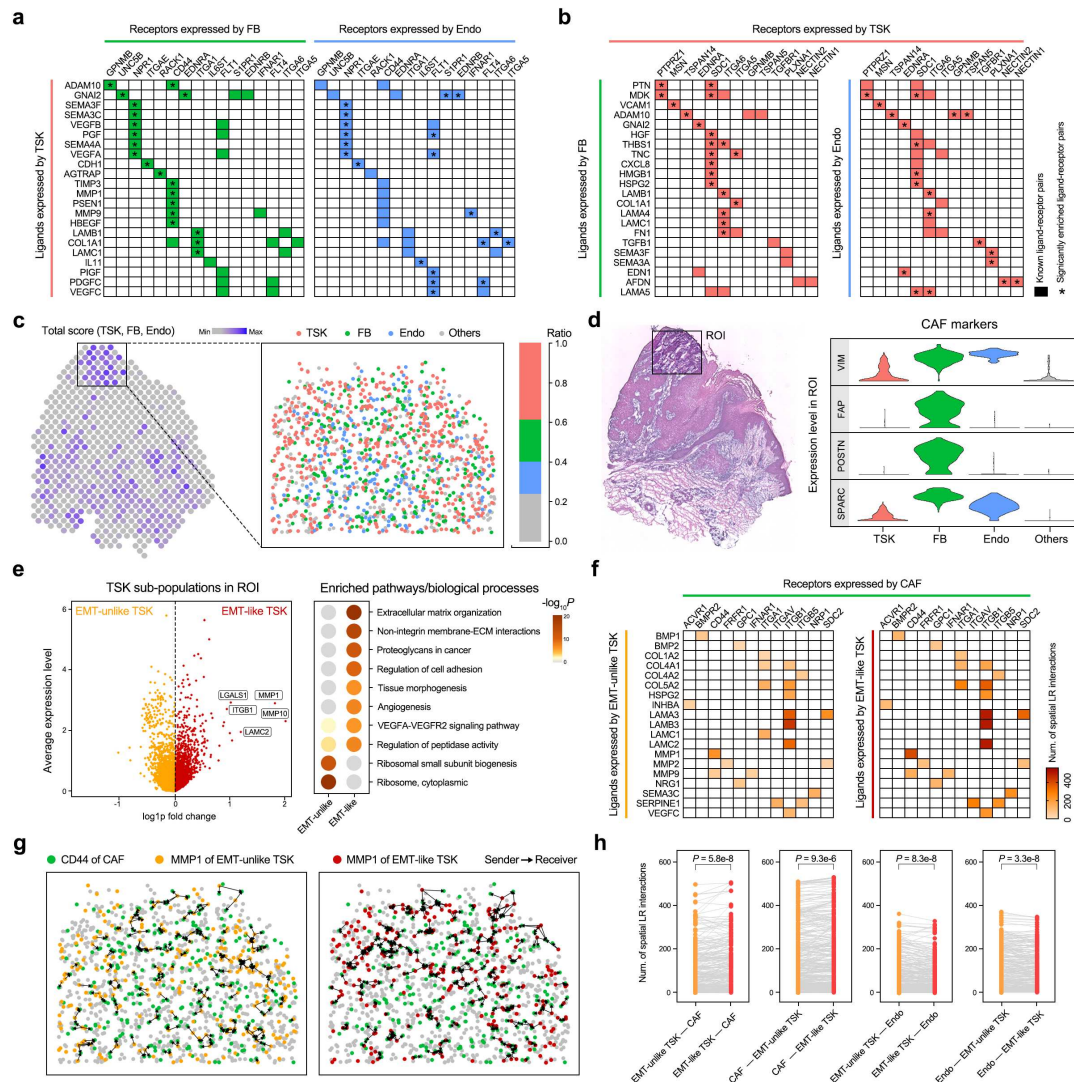

Fig. 6 Reconstruction of cell–cell communications between TSK subpopulations and stromal cells in space with SpaTalk. a Top 20 inferred LRIs that mediate cell–cell communication from the TSK senders to the FB and Endo receivers. Colored blocks represent the known ligand–receptor pairs in CellTalkDB. The asterisk represents the significantly enriched LRIs determined by SpaTalk. **b** Top 20 inferred LRIs that mediate cell–cell communication from the FB and Endo senders to TSK receivers. **c** Region of interest (ROI) covering 42 spatial spots in space with a high total score of TSK, FB, and Endo according to their signature genes. The point plot shows the decomposed single-cell ST atlas determined by SpaTalk. **d** Expression of known cancer-associated fibroblast (CAF) markers across TSKs, FB, Endo, and other cells. **e** Differentially expressed genes (DEGs) between EMT-like and EMT-unlike TSKs and the corresponding

enriched biological processes and pathways. Representative DEGs are labeled beside the point. **f** Number of cell-cell pairs over the LRIs from the EMT-like and EMT-unlike TSKs to CAFs. **g** Communications from EMT-like and EMT-unlike TSKs to CAFs mediated by the MMP1–CD44 interaction in space. **h** Comparison of communications among CAFs, Endo, EMT-like TSKs, and EMT-unlike TSKs with respect to the number of cell-cell pairs in space over the matched LRIs evaluated with a paired *t* test.

Next, we focused on a region of interest (ROI) covering 42 spatial spots in space for in-depth exploration of TSK-stroma communications, which exhibited a high total score of TSK, FB, and Endo according to their signature genes, occupying the major part in the ROI (Fig. 6c). By mapping cancer-associated fibroblast (CAF) markers to the cells in space, the majority of FB in the ROI highly expressed the known CAF marker genes (e.g., VIM, FAP, POSTIN, and SPARC) (Fig. 6d), hinting at the transformation of FB to CAFs induced by the adjacent TSKs and conversely supporting the stemness of TSKs via direct cell-cell communication in space (Supplementary Fig. 6a). Notably, the TSKs appear to be extremely heterogeneous with respect to the broad range of EMT scores in the ROI; thus, TSKs were further classified into 268 EMT-like and 268 EMT-unlike populations (Supplementary Fig. 6b). By comparing their differentially expressed genes, EMT-like TSKs were dramatically enriched with ECM organization, proteoglycans in cancer, regulation of cell adhesion, and the VEGFA-VEGFR2 signaling pathway, representing more invasive properties compared with EMT-unlike TSKs (Fig. 6e).

Additionally, EMT-like TSKs appear to be more communicative with surrounding CAFs in the TME in light of the greater number of cell-cell pairs over the LRIs that prominently mediate TSK–stroma communications in space, such as LAMB3-ITGB1, LAMA3-ITGB1, LAMC2-ITGB1, and MMP1-CD44 (Fig. 6f and Supplementary Fig. 6c, d, e). Metastasis-related laminins are essential for formation and function of the

basement membrane, whereas MMPs are involved in ECM breakdown, both contributing to the aggravated malignancy of tumors. Moreover, CD44 expression on CAFs plays a supporting role in the induction of cellular stemness, wherein CAFs have a preference of cell–cell communications with EMT-like TSKs in space (Fig. 6g). Interestingly, EMT-unlike TSKs notably exhibited more communicative cell–cell pairs with Endo, whereas EMT-like TSKs exhibited significantly more communicative cell–cell pairs with CAFs over the matched LRIs (Fig. 6h), consistent with the observed contribution of CAFs to EMT in a broad range of tumors[49, 50].

Discussion

We have demonstrated the capabilities of SpaTalk to infer and visualize spatially resolved cell–cell communications mediated by significantly enriched LRIs under normal and disease states over existing representative datasets, including the single-cell ST data generated from STARmap, MERFISH, and seqFISH+, and the spot-based ST data obtained via Slide-seq and 10X Visium.

There are two principles to decode the mechanisms of cell–cell communications: ligand-receptor proximity and LRT co-expression[12]. In a given tissue niche, cells are more likely to communicate with each other when they are spatially adjacent and activate downstream target genes in the receiving cell triggered by the LRI in proximal cells; thus, ST data are well suited to apply the two principles for inferring inter-cellular communications. Accordingly, our proposed SpaTalk realizes the integration of these two principles by incorporating the KNN and cell–cell graph network to filter spatially proximal cell pairs and corresponding LRIs, followed by utilizing the knowledge graph algorithm to model the LRT signal propagation process. Consequently, the

performance of SpaTalk was superior to that of other methods over the benchmarked ST datasets with respect to several evaluation indices, demonstrating the reliability of the two principles in decoding cellular cross-talk, especially for juxtracrine and paracrine communication.

Importantly, SpaTalk is applicable to either single-cell or spot-based ST datasets generated from mainstream ST technologies. For the former, SpaTalk assigns a label to each cell by selecting similar cell types with the top-ranked weight via NNLM for single-cell ST data, generating the ST atlas at single-cell resolution with known cell types for the subsequent inference of cell–cell communications. For spot-based ST data, SpaTalk selects and maps the optimal combination of cells in accordance with the decomposed optimal weight/percent of cell types via NNLM and the transcriptome profiles of spatial spots to reconstruct the ST atlas at single-cell resolution with known cell types. Notably, applications of SpaTalk to the mouse cortex and liver datasets sequenced by STARmap and Slide-seq, respectively, revealed the evidential LRIs in space that mediate the spatially resolved cell–cell communications contributing to normal physiological processes. Moreover, exploration of SpaTalk on the human skin SCC dataset obtained from 10X Visium identified the variable preference of communication among tumor subpopulations, CAF, and Endo. These cases convincingly demonstrate the universality of SpaTalk in decoding the mechanism of cell–cell communications in space underlying normal and disease tissues for single-cell and spot-based ST data.

As unmatched scRNA-seq and ST data would directly influence the cell-type decomposition, an important feature of SpaTalk is the ability to assign a spot/cell into an unsure category considering the unseen cell types in the scRNA-seq reference. For

example, the scRNA-seq reference for the Slide-seq mouse cortex ST data was obtained from another repository for the same tissue, resulting in numerous unsure cells by assuming one cell in each spot in terms of the high resolution (10 μm) of Slide-seq technology that almost approaches single-cell resolution. Additionally, the extremely low gene coverage of several spatial spots severely affects the regression model, which were regarded as the unsure type by SpaTalk. However, with respect to the human skin SCC datasets, SpaTalk removed the unsure type for the matched scRNA-seq and ST data. As the matched multi-modal datasets will undoubtedly become greater in number, application of SpaTalk and similar methods will be required for accurate inference of spatially resolved cell–cell communications.

Additionally, SpaTalk characterizes the spatial distribution for each cell type within the reconstructed ST at single-cell resolution through the contour plot of cellular density in space, which enables analyzing the proximal relationship between paired cell types. Moreover, SpaTalk enables the statistical analyses and visualization of spatially proximal LRIs in space, forming a dynamic cell–cell communication network. Currently, it is hard to analyze and visualize the LRI at single-cell resolution for scRNA-seq data, wherein the common practice is to interpret the LRI for paired cell types. By incorporating spatial information, SpaTalk displays the enriched LRI at single-cell resolution via the spatially proximal co-expressed cell pairs, offering an informatively brand-new approach for the analysis and visualization of the LRI and its mediated cell–cell communication underlying the disease pathology from a novel perspective, as shown in the application of SpaTalk to the human skin SCC datasets.

Adding spatial constraints in cell–cell communication inference is critical to the spatial analysis of juxtracrine and paracrine communications. However, this constraint

inevitably causes the failure of inferring long-range communications such as endocrine and telecrine signaling. Classification of LRIs into short-range and long-range communications with prior knowledge might be helpful to infer the comprehensive communication categories computationally. Moreover, it is potentially beneficial to include other omics data with the increasing multi-modal datasets generated from state-of-the-art technologies such as 10X Multiome and Digital Spatial Profiling[51] in studying spatially regulated cell–cell communications. Thus, more reliable computational models might be needed for more accurate integration of multi-modal data and inference.

Methods

Datasets. For STARmap, the single-cell ST data of the mouse cortex (20180410-BY3_1kgenes) was obtained from a public data portal (https://www.dropbox.com/sh/f7ebheru1lbz91s/AABYSSjSTppBmVmWl2H4sKa?dl=0). For MERFISH, the single-cell ST data of the naïve female mouse (Animal_ID: 1, Bregma: 0.26) hypothalamic preoptic region was downloaded from Dryad (https://datadryad.org/stash/dataset/doi:10.5061/dryad.8t8s248). For seqFISH+, the single-cell ST data of the mouse cortex and olfactory bulb were retrieved from the Github repository (https://github.com/CaiGroup/seqFISH-PLUS). For Slide-seq, the spot-based ST data of the mouse liver (Puck_180803_8) and somatosensory cortex (Puck_200306_03) were obtained from the Broad Institute Single Cell Portal (https://singlecell.broadinstitute.org/single_cell/study/SCP354/slide-seq-study) and (https://singlecell.broadinstitute.org/single_cell/study/SCP815/highly-sensitive-spatial-transcriptomics-at-near-cellular-resolution-with-slide-seqv2), respectively. For

10X Visium, the spot-based ST data and scRNA-seq data of human SCC were downloaded from the Gene Expression Omnibus (GEO) repository (GSE144240). The mouse liver scRNA-seq data of non-parenchymal and parenchymal hepatic cells were refined from the MCA (https://figshare.com/articles/MCA_DGE_Data/5435866) and GSE125688, respectively. The mouse cortex scRNA-seq data were obtained from GSE71585.

Data processing. For the liver scRNA-seq datasets, the non-parenchymal cells and parenchymal hepatic cells were collected from the MCA and GSE125688, respectively, wherein hepatocytes were classified into pericentral and periportal hepatocytes with principal component analyses and clustering analysis. For the MERFISH dataset, ependymal cells were excluded due to the limited cell number in the section (<2). For other datasets, all cells were included in the filtered matrices. Human and mouse gene symbols were revised in accordance with NCBI gene data (https://www.ncbi.nlm.nih.gov/gene/) updated on June 30, 2021, wherein unmatched genes and duplicated genes were removed. For all ST and scRNA-seq datasets, the raw counts were normalized via the global-scaling normalization method LogNormalize in preparation for running the subsequent scDeepSort pipeline.

SpaTalk algorithm. The SpaTalk model consists of two components: cell-type decomposition and spatial LRI enrichment. The first component is to infer cell-type composition for single-cell or spot-based ST data, and the second component is to infer spatially proximal ligand–receptor interactions that mediate cell–cell communications in space.

Cell-type decomposition. To dissect the cell-type composition for the ST data matrix $T[n \times s]$ (n genes and s spots/cells), NNLM was first applied to obtain the

optimal proportion of cell types using the scRNA-seq data matrix $S[n \times c]$ (n genes and c cells) as the reference with k cell types. Let $Y = \{y_1, y_2, \dots, y_n\}$ be the expression profile for each spot/cell to establish the following linear model:

$$Y = X\beta + \varepsilon$$

where $X = [n \times k]$ is the average expression profile generated from S and ε represents random error. Mean relative entropy loss was then used to measure the difference between the predicted and observed values. Therefore, the objective function can be written as:

$$argmin\,\{\beta \geq 0\}\,L(Y - X\beta) + \lambda_1 R_1(\beta) + \lambda_\alpha R_\alpha(\beta) + \lambda_2 R_2(\beta)$$

where R_1, R_α and R_2 represent the L1, angle, and L2 regularization with non-negative λ_1, λ_α and λ_2 initialized by zero[23, 24]. The model was trained with the above objective function using Lee's multiplicative iteration algorithm[25] with default hyperparameters until convergence or after 10,000 iterations to generate the coefficient matrix $C[k \times s]$.

For single-cell ST data, the cell type with the maximum coefficient was assigned to each cell. For spot-based ST data, let M be the maximum cell number for each spot, which was set to 30 for 10X Visium data and was set to 1 for Slide-seq data according to a recent review. In practice, the optimal cellular combination ω for each spot was determined by the following function:

$$\omega_i\,(i \in \{1, 2, \dots, k\}) = \begin{cases} [M\beta_i] + 1 & (\{M\beta_i\} \geq 0.5) \\ [M\beta_i] & (\{M\beta_i\} < 0.5) \end{cases}$$

wherein $[M\beta_i]$ and $\{M\beta_i\}$ represent the integer and fractional parts of $M\beta_i$, respectively. For each spot, we randomly selected m $(m = \sum_{i=1}^{k} \omega_i)$ cells from S to compare their merged expression profile ϵ with the ground truth according to the

following function:

$$argmin\,\{m \leq M\} \sum_{i=1}^{n} (Y_i - \sum_{j=1}^{m} \epsilon_i^j)^2$$

To assign a coordinate $(x,\ y)$ to each sampled cell, we applied stochastic $\alpha \in [0,\ 1]$ and $\theta \in [0,\ 360]$ in spot $(x_0,\ y_0)$ to locate the cell into the space detailed in the following function:

$$x = x_0 + \alpha d_{min} \cos(\theta\pi/180)$$
$$y = y_0 + \alpha d_{min} \sin(\theta\pi/180)$$

where d_{min} represents the spatial distance of the closest neighbor spot. By integrating the optimal cellular combinations for all spots, ST data at single-cell resolution were reconstructed for the spot-based ST data.

Spatial LRI enrichment. To generate the cell–cell distance matrix D, the Euclidean distance between cells was calculated using the single-cell spatial coordinates of ST data. The KNN algorithm was then applied to each cell to select the *K* nearest cells from D to construct the cell graph network. For ligand *i* of the sender (cell type A) and receptor *j* of the receiver (cell type B), the number of LRI pairs ($P_{Ai,Bj}^0$) was obtained from the graph network by counting the 1-hop neighbor nodes of receivers for each sender. The permutation test was then performed by randomly shuffling cell labels to recalculate the number of LRI pairs. By repeating this step Z times, a background distribution $P = \{P_{Ai,Bj}^1,\ P_{Ai,Bj}^2, \dots,\ P_{Ai,Bj}^Z\}$ was obtained for comparison with the real interacting score, and the P value was calculated as follows:

$$P_{Ai,Bj} = crad\{x \in P \mid x \geq P_{Ai,Bj}^0\}/Z$$

where $P_{Ai,Bj}$ values less than 0.05 were filtered to calculate the intercellular score of LRI from senders to receivers ($S_{Ai,Bj}^{inter} = 1 - P_{Ai,Bj}$). To further enrich the LRIs that activate downstream TFs, target genes, and the related pathways of receivers, the

knowledge graph was introduced to model the intracellular signal propagation process. In practice, LRIs from CellTalkDB, pathways from KEGG and Reactome, and TFs from AnimalTFDB were integrated to construct the ligand–receptor–TF knowledge graph (LRT-KG), wherein the weight between entities represents the co-expressed coefficient. Taking the receptor as the query node, we incorporated the random-walk algorithm into the LRT-KG to filter and score the downstream activated t TFs with no more than 10 steps and Z iterations; thus, the probability p for each TF can be calculated with the ratio of successful hits from the query node to the target TF during the Z random walks. By integrating the co-expressed TFs and the corresponding target genes from the LRT-KG, the intracellular score of LRI from senders to receivers can be written as:

$$S_{Ai,Bj}^{intra} = \sum_{k=1}^{t} \theta_k \times p_k / \eta_k$$

where θ represents the number of targeted genes, η represents the step from the receptor to the TF in the LRT-KG. By the sigmoid transformation for $S_{Ai,Bj}^{intra}$, the final score of the LRI from cell type A to cell type B can be written as:

$$S_{Ai,Bj} = \sqrt{S_{Ai,Bj}^{inter} \times S_{Ai,Bj}^{intra}}$$

Comparison with other methods. STARmap, MERFISH, and seqFISH+ ST data were used to compare the performance of SpaTalk with other existing cell-type decomposition methods. For these single-cell ST data, all cells were split according to the fixed spatial distance and then merged into simulated spots as the benchmark datasets. RCTD, SPOTlight, Seurat, deconvSeq, and Stereoscope were benchmarked with the default parameters and evaluated with Pearson's correlation coefficient and RMSE over the predicted and real cell-type composition for each spot.

Given the limited genes of MERFISH ST data, STARmap and seqFISH+ single-cell ST

data (including 1020 and 10,000 genes, respectively) were used as the benchmark datasets to compare the performance of SpaTalk with other cell–cell communication inference methods (Giotto, SpaOTsc, NicheNet, CytoTalk, and CellCall). The one-sided Wilcoxon test was performed to evaluate the spatial proximity significance of the inferred LRIs by comparing the number of expressed LRIs between sender–receiver pairs and all cell–cell pairs, and the co-expressed percent of the LRI was calculated to evaluate the co-expression level by counting the number of expressed LRIs from senders to receivers from the cell–cell graph network. All methods were benchmarked with the default parameters and all inferred LRIs were unbiasedly evaluated with the above criteria except for the LRIs from SpaOTsc since the number of inferred LRIs was much larger than that of the other methods; thus, the top 1000 LRIs for each cell–cell communication were selected from SpaOTsc according to the final score. Given the significantly enriched biological processes or pathways in the receiver cell type, the Fisher exact test was adopted for pathway enrichment analysis with the KEGG and Reactome databases on the activated genes in receivers using the following function:

$$ P = \binom{a+b}{a} \binom{c+d}{c} / \binom{n}{a+c} $$

where $n = a + b + c + d$; a is the number of inferred target genes that match a given pathway, b is the number of given pathway genes that exclude a, c is the number of inferred target genes that unmatch a given pathway, and d is the number of all genes excluding a, b, and c. NicheNet, CytoTalk, and CellCall were benchmarked with the default parameters and the inferred target genes for each LRI were evaluated according to the significance of pathway enrichment.

Pathway and biological process enrichment. The Metascape web tool

(https://metascape.org/) was used to perform the enrichment analysis of pathways and biological processes, wherein the top 100 highly expressed genes were selected according to the fold change of the average gene expression. Gene Set Enrichment Analysis (GSEA) was performed using the ranked gene list with the clusterprofiler tool to enrich the significantly activated pathways and biological processes, whose signatures were obtained from the Molecular Signatures Database v7.4 (MSigDB, http://www.gsea-msigdb.org/gsea/msigdb), including the gene sets from Gene Ontology (GO) and the canonical pathway gene sets derived from the KEGG, Reactome, and WikiPathways pathway databases.

Module scoring of hallmarks and signatures. Hallmark scoring of metabolism of xenobiotics by cytochrome P450, synthesis of bile acids and bile salts, TSK, and EMT was performed using the "AddModuleScore" function in Seurat with default parameters. Hallmark pathways and EMT were obtained from MSigDB, and the signature genes of the TSK were download from the original publication by Jin et al.

Statistics. R (version 4.1.1) and GraphPad Prism 8 were used for all statistical analyses.

Data and code availability

No new data was generated for this study. All data used in this study is publicly available as previously described. Source codes for the SpaTalk R package and the related scripts are available at github (https://github.com/ZJUFanLab/SpaTalk).

Acknowledgements

Author contributions

X.F., X.X., and H.C. conceived and designed the study. C.L., X.L., J.L., J.Q., and K.W. collected and analyzed the scRNA-seq and ST data. X.S., H.Y., J.C, and P.Y. implemented the algorithm of SpaTalk. X.S., C.L., and H.Y. developed the package of SpaTalk. All authors wrote the manuscript, read and approved the final manuscript.

Competing interests

The authors declare no competing interests.

Reference

1. Shao X, Lu X, Liao J, Chen H, Fan X. New avenues for systematically inferring cell-cell communication: through single-cell transcriptomics data. *Protein Cell* **11**, 866-880 (2020).
2. Armingol E, Officer A, Harismendy O, Lewis NE. Deciphering cell-cell interactions and communication from gene expression. *Nat Rev Genet* **22**, 71-88 (2021).
3. Shao X*, et al.* scDeepSort: a pre-trained cell-type annotation method for single-cell transcriptomics using deep learning with a weighted graph neural network. *Nucleic Acids Res* **49**, e122 (2021).
4. Cabello-Aguilar S, Alame M, Kon-Sun-Tack F, Fau C, Lacroix M, Colinge J. SingleCellSignalR: inference of intercellular networks from single-cell transcriptomics. *Nucleic Acids Res* **48**, e55 (2020).
5. Jung S, Singh K, Del Sol A. FunRes: resolving tissue-specific functional cell states based on a cell-cell communication network model. *Brief Bioinform* **22**,   (2021).
6. Browaeys R, Saelens W, Saeys Y. NicheNet: modeling intercellular communication by linking ligands to target genes. *Nat Methods* **17**, 159-162 (2020).
7. Hu Y, Peng T, Gao L, Tan K. CytoTalk: De novo construction of signal transduction networks using single-cell transcriptomic data. *Sci Adv* **7**,   (2021).

8.   Zhang Y, *et al.* CellCall: integrating paired ligand-receptor and transcription factor activities for cell-cell communication. *Nucleic Acids Res* **49**, 8520-8534 (2021).

9.   Zhang M, *et al.* Spatial molecular profiling: platforms, applications and analysis tools. *Brief Bioinform* **22**,   (2021).

10.   Lein E, Borm LE, Linnarsson S. The promise of spatial transcriptomics for neuroscience in the era of molecular cell typing. *Science* **358**, 64-69 (2017).

11.   Liao J, Lu X, Shao X, Zhu L, Fan X. Uncovering an Organ's Molecular Architecture at Single-Cell Resolution by Spatially Resolved Transcriptomics. *Trends Biotechnol* **39**, 43-58 (2021).

12.   Longo SK, Guo MG, Ji AL, Khavari PA. Integrating single-cell and spatial transcriptomics to elucidate intercellular tissue dynamics. *Nat Rev Genet* **22**, 627-644 (2021).

13.   Moss A, *et al.* A single cell transcriptomics map of paracrine networks in the intrinsic cardiac nervous system. *iScience* **24**, 102713 (2021).

14.   Stur E, *et al.* Spatially resolved transcriptomics of high-grade serous ovarian carcinoma. *iScience* **25**, 103923 (2022).

15.   Almet AA, Cang Z, Jin S, Nie Q. The landscape of cell-cell communication through single-cell transcriptomics. *Curr Opin Syst Biol* **26**, 12-23 (2021).

16.   Dries R, *et al.* Giotto: a toolbox for integrative analysis and visualization of spatial expression data. *Genome Biol* **22**, 78 (2021).

17.   Cang Z, Nie Q. Inferring spatial and signaling relationships between cells from single cell transcriptomic data. *Nat Commun* **11**, 2084 (2020).

18.   Mohamed SK, Nounu A, Novacek V. Biological applications of knowledge graph embedding models. *Brief Bioinform* **22**, 1679-1693 (2021).

19.   Wang X, *et al.* Three-dimensional intact-tissue sequencing of single-cell transcriptional states. *Science* **361**,   (2018).

20.   Rodriques SG, *et al.* Slide-seq: A scalable technology for measuring genome-wide expression at high spatial resolution. *Science* **363**, 1463-1467 (2019).

21.   Stickels RR, *et al.* Highly sensitive spatial transcriptomics at near-cellular resolution with Slide-seqV2. *Nat Biotechnol* **39**, 313-319 (2021).

22.   Ji AL, *et al.* Multimodal Analysis of Composition and Spatial Architecture in Human Squamous Cell Carcinoma. *Cell* **182**, 497-514 e422 (2020).

23.   Pascual-Montano A, Carazo JM, Kochi K, Lehmann D, Pascual-Marqui RD. Nonsmooth nonnegative matrix factorization (nsNMF). *IEEE Trans Pattern Anal Mach Intell* **28**, 403-415 (2006).

24.   Franc V, Hlaváč V, Navara M. Sequential Coordinate-Wise Algorithm for the Non-negative Least Squares Problem. In: *Computer Analysis of Images and Patterns* (eds Gagalowicz A, Philips W). Springer Berlin Heidelberg (2005).

25.   Lee DD, Seung HS. Learning the parts of objects by non-negative matrix factorization. *Nature* **401**, 788-791 (1999).

26.   Shao X, Liao J, Li C, Lu X, Cheng J, Fan X. CellTalkDB: a manually curated database of ligand-receptor interactions in humans and mice. *Brief Bioinform* **22**,   (2021).

27.   Hu H, Miao YR, Jia LH, Yu QY, Zhang Q, Guo AY. AnimalTFDB 3.0: a comprehensive resource for annotation and prediction of animal transcription factors. *Nucleic Acids Res* **47**, D33-D38 (2019).

28.   Lee B, Zhang S, Poleksic A, Xie L. Heterogeneous Multi-Layered Network Model for Omics

Data Integration and Analysis. *Front Genet* **10**, 1381 (2019).

29.   Moffitt JR*, et al.* Molecular, spatial, and functional single-cell profiling of the hypothalamic preoptic region. *Science* **362**,   (2018).

30.   Eng CL*, et al.* Transcriptome-scale super-resolved imaging in tissues by RNA seqFISH. *Nature* **568**, 235-239 (2019).

31.   Cable DM*, et al.* Robust decomposition of cell type mixtures in spatial transcriptomics. *Nat Biotechnol*,   (2021).

32.   Stuart T*, et al.* Comprehensive Integration of Single-Cell Data. *Cell* **177**, 1888-1902 e1821 (2019).

33.   Elosua-Bayes M, Nieto P, Mereu E, Gut I, Heyn H. SPOTlight: seeded NMF regression to deconvolute spatial transcriptomics spots with single-cell transcriptomes. *Nucleic Acids Res* **49**, e50 (2021).

34.   Du R, Carey V, Weiss ST. deconvSeq: deconvolution of cell mixture distribution in sequencing data. *Bioinformatics* **35**, 5095-5102 (2019).

35.   Andersson A*, et al.* Single-cell and spatial transcriptomics enables probabilistic inference of cell type topography. *Commun Biol* **3**, 565 (2020).

36.   Tasic B*, et al.* Shared and distinct transcriptomic cell types across neocortical areas. *Nature* **563**, 72-78 (2018).

37.   Dipoppa M, Ranson A, Krumin M, Pachitariu M, Carandini M, Harris KD. Vision and Locomotion Shape the Interactions between Neuron Types in Mouse Visual Cortex. *Neuron* **98**, 602-615 e608 (2018).

38.   Krieglstein K, Zheng F, Unsicker K, Alzheimer C. More than being protective: functional roles for TGF-beta/activin signaling pathways at central synapses. *Trends Neurosci* **34**, 421-429 (2011).

39.   Allen NJ, Lyons DA. Glia as architects of central nervous system formation and function. *Science* **362**, 181-185 (2018).

40.   Sun M, Gewirtz JC, Bofenkamp L, Wickham RJ, Ge H, O'Connor MB. Canonical TGF-beta signaling is required for the balance of excitatory/inhibitory transmission within the hippocampus and prepulse inhibition of acoustic startle. *J Neurosci* **30**, 6025-6035 (2010).

41.   Tasic B*, et al.* Adult mouse cortical cell taxonomy revealed by single cell transcriptomics. *Nat Neurosci* **19**, 335-346 (2016).

42.   Han X*, et al.* Mapping the Mouse Cell Atlas by Microwell-Seq. *Cell* **172**, 1091-1107 e1017 (2018).

43.   Pepe-Mooney BJ*, et al.* Single-Cell Analysis of the Liver Epithelium Reveals Dynamic Heterogeneity and an Essential Role for YAP in Homeostasis and Regeneration. *Cell Stem Cell* **25**, 23-38 e28 (2019).

44.   Shao X, Liao J, Lu X, Xue R, Ai N, Fan X. scCATCH: Automatic Annotation on Cell Types of Clusters from Single-Cell RNA Sequencing Data. *iScience* **23**, 100882 (2020).

45.   Yuan Z*, et al.* SEAM is a spatial single nuclear metabolomics method for dissecting tissue microenvironment. *Nat Methods* **18**, 1223-1232 (2021).

46.   Ben-Moshe S, Itzkovitz S. Spatial heterogeneity in the mammalian liver. *Nat Rev Gastroenterol Hepatol* **16**, 395-410 (2019).

47.   Margadant C, Sonnenberg A. Integrin-TGF-beta crosstalk in fibrosis, cancer and wound healing. *EMBO Rep* **11**, 97-105 (2010).

48. Chen CH, Chen WY, Lin SF, Wong RJ. Epithelial-mesenchymal transition enhances response to oncolytic herpesviral therapy through nectin-1. *Hum Gene Ther* **25**, 539-551 (2014).

49. Wen S*, et al.* Cancer-associated fibroblast (CAF)-derived IL32 promotes breast cancer cell invasion and metastasis via integrin beta3-p38 MAPK signalling. *Cancer Lett* **442**, 320-332 (2019).

50. Asif PJ, Longobardi C, Hahne M, Medema JP. The Role of Cancer-Associated Fibroblasts in Cancer Invasion and Metastasis. *Cancers (Basel)* **13**,   (2021).

51. Merritt CR*, et al.* Multiplex digital spatial profiling of proteins and RNA in fixed tissue. *Nat Biotechnol* **38**, 586-599 (2020).